nature photonics

FOCUS | REVIEW ARTICLES

PUBLISHED ONLINE: 30 JULY 2010 | DOI: 10.1038/NPHOTON.2010.185

Nonlinear silicon photonics

J. Leuthold*, C. Koos and W. Freude

Silicon offers an abundance of nonlinear optical effects that can be used to generate and process optical signals in low-cost ultracompact chips at speeds beyond those of today's electronic devices. The Review discusses the nonlinear optical effects in silicon and highlights some of the associated key applications.

Silicon offers a variety of nonlinear effects that can be used to process optical signals at speeds of 100 Gbit s^{-1} and beyond[1–5], detect signals at unprecedented sensitivities for novel sensing applications[6,7] and enable broadband electro-optic modulation[8–11]. Ultimately, the nonlinear effects in silicon may also permit the generation of photons for lasing and amplification[12–15]. It should be mentioned, however, that although these nonlinear effects are numerous, the interest in nonlinear silicon photonics is not so much due to the superior nonlinear characteristics of silicon over alternative integrated-optics materials, but rather because of its potentially lower cost and high compatibility with CMOS industry, which is interested in combining new optical functionalities with electronics on a single chip.

The challenges in the development of active silicon elements are: (1) the indirect minimum-energy bandgap of silicon, which makes spontaneous emission unlikely and thus impedes lasing; (2) the centrosymmetry of the silicon crystal, which prevents electro-optic effects and thus hinders the development of electro-optic silicon modulators; and (3) the variety of fast and slow higher-order nonlinear effects that result in both slow and fast recovery times when the material is exposed to high field strengths or sudden temporal changes. Despite these issues, there has been impressive progress in the development of functional nonlinear silicon photonic devices. Today, silicon devices can emit light, modulate signals electro-optically and process data at speeds higher than electronic chips. This success is partially due to sophisticated technical solutions, and in particular has been enabled by progress in the fabrication of nanophotonic devices[16,17].

The goal of this Review is to summarize the wealth of nonlinear effects found in silicon, and to highlight selected applications and technological solutions that have emerged during the past few years. First, a short summary of silicon is given, following which the various nonlinear effects and specific techniques used in the application of these techniques are reviewed. Finally, a selected number of applications are discussed in more detail.

The vision

Silicon is the raw material for the silicon-on-insulator (SOI) platform, a fabrication approach in which a thin silicon layer on top of an insulator layer resides on a silicon substrate. The functional optical elements are situated in the thin top-silicon layer, and the insulator is typically made from SiO_2. The refractive index of waveguiding silicon is high ($n_{Si} = 3.48$) compared with air ($n = 1$) or the SiO_2 cladding layer ($n_{SiO_2} = 1.44$), and hence strong optical guiding is guaranteed for all signals around the typical near-infrared wavelength of 1,550 nm.

The SOI platform has become the foundation of silicon photonics for many good reasons[18–20]. For example, silicon is widely available and is compatible with mature CMOS technology, thus offering structure sizes down to 10 nm at low cost[21,22]. The strong optical confinement of silicon allows for very compact optical devices with bent waveguide radii of the order of a few micrometres, and functional waveguide elements of ten to a few hundred micrometres. Consequently, large-scale integration of many functional elements on a single chip is within reach[16].

Silicon photonics also extends to highly integrated multifunctional devices that perform both optical and electrical operations on a single low-cost chip. Such devices could replace the large network interface cards that interconnect optical communications networks with computers, or could act as sensitive optical detectors with built-in processors for pre-processing detected signals. Other applications include the development of silicon photonic circuits for optical chip-to-chip communications[23] and the development of silicon highest-speed signals processors for optical communications and computers[24]. Besides passive splitters, filters and multiplexers, such chips could also potentially comprise active elements such as lasers, amplifiers, modulators, signal regenerators and wavelength converters. Slow-light photonic crystals could be used to enhance the nonlinear effects, and third-harmonic generation could be used for monitoring applications[25].

Nonlinear effects in silicon

There are a plethora of nonlinearities in silicon[26–28], and they all originate from the interactions of the optical field with electrons and phonons. In fact, it is the electric field of the optical signal that resonates with the electrons in the outer shells of the silicon atoms and thus causes polarization. Figure 1a illustrates how a photon oscillating at frequency ω polarizes an atom by displacing an electron orbital with respect to the nucleus. In its simplest form, and assuming an instantaneous dielectric response in an isotropic material, the relation between an induced polarization ($P(t)$, scalar) and an electric field ($E(t)$, also scalar) is expressed by a power series in the electric field[26]:

$$P(t) = \varepsilon_0(\chi^{(1)}E(t) + \chi^{(2)}E^2(t) + \chi^{(3)}E^3(t) + \ldots) \quad (1)$$

where ε_0 is the vacuum permittivity and $\chi^{(i)}$ are the ith-order optical susceptibilities. The susceptibility terms are tensors of rank $(i + 1)$, and describe whether the relation between the induced polarization is linear or nonlinear, whether the electric fields induce phase-shifts, absorb or amplify the incident field, and whether waves at new frequencies are generated. Here, the nonlinear effects associated with each of these susceptibility coefficients are discussed, taking them to be scalars for simplicity.

$\chi^{(1)}$ processes. The complex first-order susceptibility term $\chi^{(1)}$ concerns dipole excitations with bound and free electrons induced by a single photon. The real part of $\chi^{(1)}$ is associated with the real part of the refractive index, whereas the imaginary part of $\chi^{(1)}$ describes loss or gain. Some of the dipole excitations associated

Institute of Photonics and Quantum Electronics, Karlsruhe Institute of Technology, 76131 Karlsruhe, Germany. *e-mail: juerg.leuthold@kit.edu

NATURE PHOTONICS DOI: 10.1038/NPHOTON.2010.185

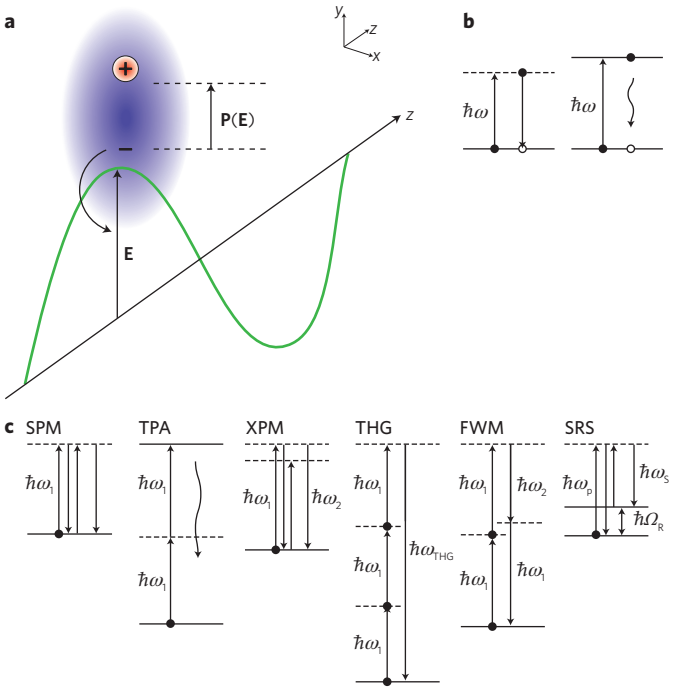

Figure 1 | Illustration of a dipole excitation and possible energy level diagrams. a, An electromagnetic wave with electric field **E** passing through an atom and thereby inducing a dipole oscillation **P**(**E**). **b**, Energy level diagrams showing possible single-photon dipole transitions with contributions to refractive index changes (left) or to free-carrier absorption (right). **c**, Third-order nonlinear dipole transitions, showing self-phase modulation (SPM), two-photon absorption (TPA), cross-phase modulation (XPM), third-harmonic generation (THG), partially degenerate and non-degenerate four-wave mixing (FWM) and stimulated Raman scattering (SRS).

with $\chi^{(1)}$ processes are depicted in Fig. 1b. The left-hand energy level diagram suggests that the refractive index has its origin in atomic dipole oscillations between a bound state and a virtual level (an energy level that does not correspond to an excited energy eigenstate of the atom[26]). Lorentz developed a simple model for calculating the contribution of bound electrons to the susceptibility, and showed that the refractive index changes strongly near a resonance. His model gives the susceptibility of bound states belonging to a density of N dipoles (elementary charge q, effective mass m_e and oscillating charge) as:

$$\chi^{(1)}_{\text{Lorentz}} = \frac{\omega_L^2}{\omega_0^2 - \omega^2 + i\gamma_L\omega} \tag{2}$$

where ω_0 is the resonance frequency of the bound state and γ_L is the associated damping constant. ω_L is the Lorentz plasma frequency, which is defined as:

$$\omega_L^2 = \frac{Nq^2}{\varepsilon_0 m_e}$$

An additional contribution to the susceptibility comes from free carriers, which semiconductors have many of at room temperature. Free carriers absorb photons and contribute to the refractive index. An absorption process with successive non-radiative recombination is depicted in the right-hand energy level diagram of Fig. 1b. The complex susceptibility induced by free carriers may be derived from equation (2) by dropping the restoring force (that is, $\omega_0 = 0$). This is described by the Drude model:

$$\chi^{(1)}_{\text{Drude}} = \frac{\omega_p^2}{-\omega^2 + i\gamma_D\omega} \tag{3}$$

with the plasma frequency ω_p being defined as:

$$\omega_p^2 = \frac{Nq^2}{\varepsilon_0 m_e}$$

Here, the plasma frequency ω_p and damping constant γ_D have different values than the corresponding quantities ω_L and γ_L in equation (2). Any contribution from either bound- or free-electron oscillations contributes to the complex refractive index. Thus, for non-magnetic materials, one may write:

$$n^2 = 1 + \chi^{(1)}_{\text{Lorentz}} + \chi^{(1)}_{\text{Drude}} \tag{4}$$

Equation (4) shows that the refractive index changes with both wavelength and carrier concentration N. Although equation (4) does provide physical insight, in practice when performing simulations researchers prefer to fit their models with directly measured wavelength dependences and free-carrier contributions from electrons (concentration N_e) and holes (concentration N_h) to the refractive index. A useful empirical function for giving the refractive index n as a function of wavelength (λ), N_e and N_h is given by:

$$n(\lambda,N_e,N_h) = n_0(\lambda) + \Delta n_f(N_e,N_h) - i\frac{\lambda}{4\pi}\Delta\alpha_f(N_e,N_h)$$

where $n_0(\lambda)$ is the wavelength dependence of the refractive index, Δn_f is the free-carrier index (FCI) change and $\Delta\alpha_f$ is the free-carrier absorption (FCA) change. $n_0(\lambda)$ for silicon is incorporated through the Sellmeier relation:

$$n_0^2(\lambda) = \varepsilon + \frac{A}{\lambda^2} + \frac{B\lambda_1^2}{\lambda^2 - \lambda_g^2} \tag{5}$$

with $\varepsilon = 11.686$, $A = 0.9398\ \mu m^2$, $B = 8.1046 \times 10^{-3}$ and the bandgap wavelength of silicon $\lambda_g = 1.1071\ \mu m$ (refs 27,29). The closer the photon gets to the bandgap energy of silicon (1.12 eV), the stronger the change in refractive index becomes. Equation (5) describes what is known as the material dispersion of silicon. Further below we will see that a precise knowledge of the material dispersion and the ability to engineer the waveguide dispersion will be instrumental in optimizing the conversion efficiency of higher-order nonlinear effects[30].

The changes in FCI and FCA at $\lambda = 1{,}550$ nm are often incorporated by the following empirical expressions[27,31]:

$$\Delta n_f = -\left[8.8\times10^{-4}\frac{N_e}{\text{cm}^{-3}} + 8.5\left(\frac{N_h}{\text{cm}^{-3}}\right)^{0.8}\right]\times10^{-18}$$

$$\frac{\Delta\alpha_f}{\text{cm}^{-1}} = -\left[8.5\frac{N_e}{\text{cm}^{-3}} + 6.0\frac{N_h}{\text{cm}^{-3}}\right]\times10^{-18}$$

where N_e and N_h have units of cm^{-3} and α_f has units of cm^{-1}.

$\chi^{(2)}$ processes. The second-order susceptibility term $\chi^{(2)}$ is absent in centrosymmetric crystals such as silicon. However, such nonlinear effects would be highly desirable as they would allow the creation of electro-optic modulators. Measures to overcome this deficiency include breaking the crystal symmetry by depositing straining

layers on top of silicon[32], or using another $\chi^{(2)}$-nonlinear electro-optic active material as a cladding[33–35]. At this point it should be mentioned that electrical modulation has also been successfully demonstrated by simply injecting and removing carriers, thereby making use of the aforementioned $\chi^{(1)}$-related FCA and FCI effects[8,36–39]. However, $\chi^{(2)}$ electro-optical modulators would be preferred as they do not suffer from carrier-related speed limitations.

$\chi^{(3)}$ processes. Third-order nonlinearities are especially important in silicon as they exhibit a wide variety of phenomena. This can be easily demonstrated for an electric field **E** comprising three frequency components (ω_k):

$$\mathbf{E}(\mathbf{r},t)=\sum_{k=1}^{3}\mathbf{E}_k=\frac{1}{2}\sum_{k=1}^{3}(\mathbf{E}_{\omega_k k}(\mathbf{r},\omega_k)e^{i\omega_k t}+c.c.) \qquad (6)$$

where *c.c.* denotes the complex conjugate. By substituting equation (6) into equation (1) and expanding the frequency components of the third-order nonlinear term $\chi^{(3)}$, one obtains a multitude of terms at new frequencies for the third-order polarization $P^{(3)}$:

$$\begin{aligned}
P^{(3)} &= \tfrac{3}{4}\varepsilon_0\chi^{(3)}[|\mathbf{E}_{\omega_1}|^2\,\mathbf{E}_1+\therefore] && \text{SPM}\\
&+\tfrac{6}{4}\varepsilon_0\chi^{(3)}[(|\mathbf{E}_{\omega_2}|^2+|\mathbf{E}_{\omega_3}|^2)\mathbf{E}_1+\therefore] && \text{XPM}\\
&+\tfrac{1}{4}\varepsilon_0\chi^{(3)}[(\mathbf{E}^3_{\omega_1}e^{i3\omega_1 t}+c.c.)+\therefore] && \text{THG}\\
&+\tfrac{3}{4}\varepsilon_0\chi^{(3)}[\tfrac{1}{2}(\mathbf{E}^2_{\omega_1}\mathbf{E}_{\omega_2}e^{i(2\omega_1+\omega_2)t}+c.c.)+\therefore] && \text{FWM} \qquad (7)\\
&+\tfrac{3}{4}\varepsilon_0\chi^{(3)}[\tfrac{1}{2}(\mathbf{E}^2_{\omega_1}\mathbf{E}^*_{\omega_2}e^{i(2\omega_1-\omega_2)t}+c.c.)+\therefore] && \text{FWM}\\
&+\tfrac{6}{4}\varepsilon_0\chi^{(3)}[\tfrac{1}{2}(\mathbf{E}_{\omega_1}\mathbf{E}_{\omega_2}\mathbf{E}^*_{\omega_3}e^{i(\omega_1+\omega_2-\omega_3)t}+c.c.)+\therefore] && \text{FWM}\\
&+\tfrac{6}{4}\varepsilon_0\chi^{(3)}[\tfrac{1}{2}(\mathbf{E}_{\omega_1}\mathbf{E}_{\omega_2}\mathbf{E}_{\omega_3}e^{i(\omega_1+\omega_2+\omega_3)t}+c.c.)+\therefore] && \text{FWM}
\end{aligned}$$

where the symbol $\therefore$ stands for all possible permutations of frequencies. Each of the terms on the right-hand side of equation (7) corresponds to a nonlinear optical excitation, of which a few are visualized in Fig. 1c. The energy level diagrams show how three photons induce dipole transitions to excited states, which subsequently relax back by releasing a fourth photon. If the excited states do not correspond to bound eigenstates of the crystal then the relaxation processes take place almost instantaneously. It is these fast processes that have caught the interest of the research community, and in fact many of the processes depicted in Fig. 1c are ultrafast. Among the many nonlinear processes, only those that maintain both energy and momentum conservation (known as phase-matching) result in efficient excitation[26]. A particular process among the many nonlinear processes available can be selected to some degree by choosing the energy levels and phase-matching appropriately.

The first term in equation (7) corresponds to a phenomenon called self-phase modulation (SPM), which results from dipole excitations induced by three photons (for example, all at an angular frequency of ω_1). This process is depicted in Fig. 1c. SPM leads to an intensity-dependent refractive index change n_2, which in turn modifies the spectral composition of the very same pulse that has generated it. As a consequence, SPM leads to a broadening of the pulse spectrum. Extreme levels of SPM may generate a supercontinuum, which has, for example, applications in the generation of ultrashort pulses in spectroscopy, telecommunications and metrology.

The photons that generate SPM can also excite an energetically higher state, as depicted in the two-photon absorption (TPA) diagram of Fig. 1c. TPA excitations are 'absorbing' because they correspond energetically to an excitation of an electron in the valence band to the conduction band. TPA leads to an intensity-dependent contribution α_2 to the linear absorption coefficient α_0. TPA generates free carriers in the conduction band that subsequently act as sources for FCA and FCI changes. The long lifetime of the free carriers in the conduction band leads to long-lasting FCA and FCI processes that ultimately slow down the speed of silicon photonic devices[40,41].

The intensity-dependent refractive index and absorption changes associated with SPM and TPA affect the complex refractive index n by the relation

$$n = n_0 + n_2 I - i\frac{\lambda}{4\pi}(\alpha_0+\alpha_2 I)$$

where I is the intensity, and n_2 (the Kerr coefficient) and α_2 are interrelated with the real and complex part of the third-order susceptibility by the equations

$$n_2 = \frac{1}{cn_0^2\varepsilon_0}\frac{3}{4}\mathrm{Re}(\chi^{(3)})$$

$$\alpha_2 = \frac{-\omega}{c^2 n_0^2\varepsilon_0}\frac{3}{2}\mathrm{Im}(\chi^{(3)})$$

A figure of merit (FOM) is often used to compare the magnitude of the Kerr coefficient n_2 with the strength of the TPA coefficient α_2:

$$\mathrm{FOM}_n = \frac{1}{\lambda}\frac{n_2}{\alpha_2}$$

A large FOM is preferable, to avoid TPA-related speed limitations. For silicon, although the Kerr nonlinear coefficient is large ($n_2 = (4.5 \pm 1.5) \times 10^{-18}$ m^2 W^{-1} at 1.55 μm; ref. 42), the large TPA coefficient results in a low FOM of ~0.4 (ref. 41). The difficulty in nonlinear optics is therefore to find a material that has both a large Kerr nonlinear coefficient and a small TPA coefficient. The quantities n_2 and α_2 vary with wavelength. Relative magnitudes of these two coefficients as a function of photon energy normalized to the bandgap energy have been derived for silicon[43], using a method similar to that of an earlier approach for direct bandgap materials[44]. The silicon Kerr coefficient actually peaks at around 1.8 μm and 1.9 μm, whereas the TPA absorption coefficient decreases considerably beyond 2 μm; that is, beyond half the bandgap energy[26]. Silicon is therefore expected to show very favourable Kerr nonlinearities with a large FOM in the near-infrared, as will be discussed further below[45,46].

The second term on the right-hand side of equation (7) represents cross-phase modulation (XPM), in which a first signal at ω_1 influences a second signal at ω_2 (Fig. 1c). The refractive index change induced by XPM is twice as strong as the refractive index change induced by SPM, as can be seen by the coefficients in the respective terms for SPM and XPM in equation (7).

The third term in equation (7) describes third-harmonic generation (THG). The third harmonic allows a new signal oscillating at $\omega_{\mathrm{THG}} = 3\omega_1$ to be produced from a signal at ω_1. For example, THG can be used to generate green light from an input signal with a wavelength of 1.55 μm (ref. 47).

The remaining terms in equation (7) describe the generation of new waves through four-wave mixing (FWM), in which three incident photons generate a fourth photon at an idler frequency ω_i. The incident photons are allowed to be degenerate, with one possible

NATURE PHOTONICS DOI: 10.1038/NPHOTON.2010.185

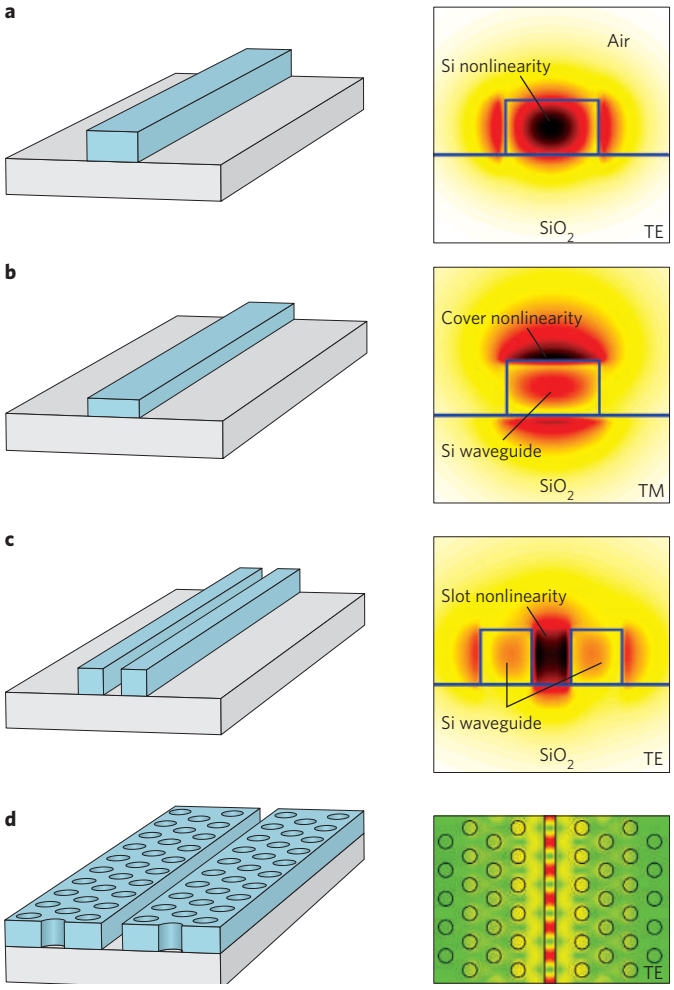

Figure 2 | Four silicon waveguide structures and their respective electric field distributions. a, Strip waveguide using silicon nonlinearity in core. **b**, Strip waveguide using cover nonlinearities. **c**, Slot waveguide using nonlinearities in the slot. **d**, Slot slow-light waveguide. The transverse electric (TE) mode has its dominant electric field component parallel to the substrate plane, whereas the transverse magnetic (TM) dominant field contribution is perpendicular to the substrate.

energy diagram shown in Fig. 1c. FWM is an ultrafast process that has a wide range of applications, for instance in wavelength conversion, parametric amplification and sampling.

A final third-order nonlinear process should be mentioned here — stimulated Raman scattering (SRS). In SRS, a pump photon is annihilated and a photon at the Stokes-shifted frequency of $\omega_S = \omega_P - \Omega_R$ is created, with $\hbar\Omega_R$ being the energy of a phonon excitation. A strong pump and a Stokes wave are needed to induce strong molecular vibrations (phonons), which in turn lead to the stimulated emission of additional Stokes waves. This allows energy to be passed on from the Raman pump to the Stokes wave. SRS has been successfully used to demonstrate amplification and lasing. In silicon, optical phonons have an energy corresponding to a frequency $\Omega_R/2\pi$ = 15.6 THz. The full-width at half-maximum (FWHM) of the phonon energy is only 105 GHz (ref. 26). As a consequence, SRS gain will take place only within a narrow 105-GHz window centred at 15.7 THz beneath the pump frequency.

Silicon photonic waveguides with a high nonlinearity

To exploit the nonlinear effects in silicon, light must first be launched into waveguides in which the nonlinear processing will take place. In this section silicon waveguide structures with particular high nonlinearities are discussed. In addition, the techniques that are frequently used to further enhance the nonlinear interactions in these waveguides will also be summarized.

The general guidelines for the design of waveguides providing particularly strong nonlinear interactions are as follows: (1) the waveguides should provide a high optical field confinement; (2) the waveguide material must have a high nonlinear Kerr coefficient; (3) the FOM should be large enough such that TPA is not an issue; and (4) where necessary, phase-matching must be guaranteed either by proper dispersion engineering or by keeping structures so short that dispersion does not matter.

A useful number to quantitatively judge the nonlinear characteristics of a particular structure is the nonlinear waveguide parameter γ, defined by

$$\gamma = \frac{2\pi}{\lambda}\frac{n_2}{A_{\mathrm{eff}}^{(3)}}$$

This parameter is maximized for large Kerr coefficients n_2 and for strongly confined modes (that is, for the smallest possible third-order nonlinear effective area $A_{\mathrm{eff}}^{(3)}$; refs 48,49). Some of the frequently used silicon waveguide structures with good mode confinement are depicted in Fig. 2, along with their corresponding electric field distributions.

Figure 2a shows the silicon strip waveguide geometry and its transverse electric field distribution. Such waveguides have typical widths ranging from 300 nm to 1.5 μm, and heights of 200 nm to 1.5 μm. The high refractive index contrast of silicon against air provides strong confinement. Nonlinear coefficients up to γ = 307,000 W^{-1} km^{-1} with an FOM of 0.4 have been measured in a 360-nm-wide and 220-nm-high strip waveguide[41]. Although this value of γ is large, the FOM is low. This means that the TPA-induced free carriers are generated with lifetimes in the nano-to-millisecond range. However, free carriers give rise to FCA and FCI effects, making fast applications impractical beyond data rates of 10 Gbit s^{-1}. Nevertheless, 10 Gbit s^{-1} all-optical processing has been shown[50]. Techniques to overcome these free-carrier-related speed-limitations include use of larger waveguides (1.5 μm × 1.5 μm) with smaller confinement and consequently lower nonlinearity coefficients, and the use of a p-i-n (p-type/intrinsic/n-type layers) diode structure across the waveguide to allow the removal of free carriers through application of a reverse bias. This method has been used to successfully demonstrate operation at 40 Gbit s^{-1} (ref. 2).

A different approach is shown in Fig. 2b, in which a silicon waveguide is covered with a nonlinear material[49]. Because the waveguide is thin, the optical transverse magnetic mode extends far into the cladding material. The idea is to choose a cladding material with both a large nonlinear Kerr coefficient n_2 and a large FOM — indeed, such a waveguide has already been fabricated and tested using DDMEBT as the nonlinear material[51,52]. The nonlinear Kerr coefficient of this organic molecule is roughly ten times larger than that of silicon, giving $n_2 = (1.7 \pm 0.8) \times 10^{-17}$ m^2 W^{-1} (ref. 51). Nonlinear coefficients of up to γ = 108,000 W^{-1} km^{-1} with a good FOM of 1.2 were found[41]. This approach — referred to as the silicon–organic hybrid (SOH) approach — takes advantage of the many organic nonlinear materials that have large Kerr coefficients[52–54]. In the future, silicon–inorganic hybrid approaches might also become important as many inorganic materials have high Kerr coefficients[55,56].

The slotted waveguide approach of Fig. 2c takes the concept of nonlinear cladding one step further[49,57,58]. In this approach, the slot not only guides the light but also enhances its intensity. The enhancement results from the continuity of the normal

component D_x of the dielectric displacement oriented parallel to the substrate plane[59]:

$$D_{x,\mathrm{Si}} = D_{x,\mathrm{slot}} \rightarrow \varepsilon_{\mathrm{Si}}\mathbf{E}_{x,\mathrm{Si}} = \varepsilon_{\mathrm{slot}}\mathbf{E}_{x,\mathrm{slot}}$$

For instance, if $n_{\mathrm{slot}} = 1.8$ and $n_{\mathrm{Si}} = 3.5$, the electric field in the slot is then enhanced by $\varepsilon_{\mathrm{Si}}/\varepsilon_{\mathrm{slot}} = (n_{\mathrm{Si}}/n_{\mathrm{slot}})^2 = 3.8$ over the electric field in the silicon, which is a significant increase. The strong field confinement inside the slot can be seen from the electric field distribution shown by the simulation in Fig. 2c. Slotted waveguide structures filled with DDMEBT provide nonlinear waveguide parameters beyond $\gamma = 116{,}000\ \mathrm{W^{-1}\ km^{-1}}$ with an excellent FOM of 2.2 and without any sign of TPA-related speed limitations[41,60].

Finally, slow-light photonic crystal waveguides[10,61,62] have also been suggested for further enhancing nonlinearities (Fig. 2d). In these structures, the slowdown of the field enhances the light–matter interaction. The third-order nonlinear phase shift enhancement is predicted to be proportional to the group index (or slowing ratio) squared, $(c/v_g)^2$ (ref. 61), whereas the second-order nonlinear enhancement is calculated to increase linearly with c/v_g (ref. 10). In these expressions c is the speed of light and v_g is the group velocity. In slow-light slot waveguides with highly nonlinear cladding, one may therefore expect to see nonlinearity enhancements due to the slow-light effect, a field enhancement due to the discontinuity of the refractive index at the slot boundaries, and advantages by the judicious choice of a material with a larger nonlinearity than silicon.

If a waveguide becomes long (several millimetres or centimetres), then walk-off and phase-matching between the pulse and probe signals or between electrical and optical waves may become an issue. In silicon waveguides such walk-off and phase-matching issues have been successfully overcome by proper engineering of the waveguide geometry. Good reports of such dispersion engineering have been given in ref. 30 and ref. 63.

The ultimate speed of nonlinear devices

The ultimate speed of a nonlinear device is often subject to controversial discussion. First, there are a multitude of nonlinear operations that each take advantage of different nonlinear aspects, making comparison quite difficult. Second, many nonlinear operations require the devices to work for an extended period of time in the linear regime, but only occasionally in the nonlinear regime. It is therefore quite tempting to cite the operation speed of the linear regime rather than that of the nonlinear regime.

For example, if nonlinear processing speeds are discussed then it is expected that the device works error-free in the nonlinear regime at the specified transmission rate for a pseudo-random bit sequence. Both the received signal quality and the pseudo-random bit sequence length must be stated. An example of such a nonlinear process is all-optical wavelength conversion, in which every single incoming bit modulated to an optical carrier is mapped to a carrier at a new wavelength. This operation must be error-free for all possible bit patterns, and this can be achieved only if the response and recovery times of the nonlinear medium are within the order of the bitrate.

Conversely, if sampling is performed then one takes advantage of the ultrafast response times to generate a short gating window, which allows extraction of a single bit from a larger bit stream. For instance, if a time-multiplexed 1 Tbit $\mathrm{s^{-1}}$ signal is successfully demultiplexed into its one tributary at 10 Gbit $\mathrm{s^{-1}}$ by means of a nonlinear process, then it proves that the device can successfully generate ultrashort gates with subpicosecond rise times. The device is therefore rightfully said to have terahertz sampling capabilities. However, nonlinear processing has only been performed at a rate of 10 GHz.

Similarly, if a nonlinear effect is seen across an optical bandwidth of several terahertz then this clearly shows the potential of the device for terahertz sampling, but it does not conclusively indicate that the device can also perform nonlinear processing at the quoted repetition rate. An actual implementation could be jeopardized by a dominant lower-speed process, and so error-free operation may not be seen. As a consequence, results obtained through statistical averaging bear no relevance to communications, in which error-free operation must be guaranteed for each and every bit.

The ultimate speed of an integrated optical device therefore strongly depends on the nonlinear operation under consideration. Additionally, other effects that depend on the actual implementation may limit the speed, such as optical carrier phase mismatch or walk-off between the optical signals themselves or between optical and electrical signals. To overcome walk-off and phase-mismatch limitations, dispersion engineering might help[30,63]. Other limitations might be inherent to the material. For example, bandwidth limitations in silicon are encountered with the Raman effect, which is only found across a limited optical window of 105 GHz (ref. 26). Other material-related speed limitations in silicon are often due

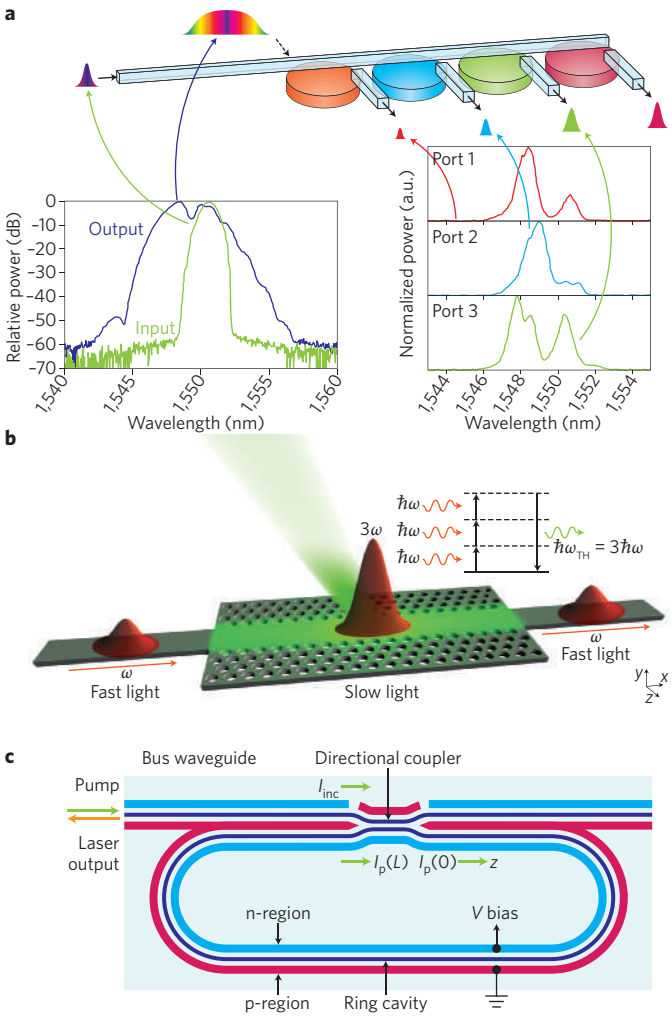

Figure 3 | Nonlinear silicon light sources. a, A short input pulse is spectrally broadened in a nonlinear silicon wire waveguide using SPM and subsequently distributed to several outputs, each at different wavelengths. **b**, Using THG to generate green light in a slow-light silicon photonic crystal waveguide. **c**, A silicon Raman ring laser within a ring laser cavity. A reverse-bias p-i-n structure is placed across the silicon rib waveguide to 'sweep out' TPA-induced carriers. Figure reproduced with permission from: **a**, ref. 72, © 2007 AIP; **b**, ref. 47, © 2009 NPG; **c**, ref. 84, © 2007 NPG.

to carrier-induced TPA, FCI and FCA effects. The time constants of these effects are typically of the order of several hundred picoseconds to several hundred nanoseconds[41]. Measures to overcome material-related speed limitations involve active carrier removal[14], the usage of larger waveguide cross-sections to stay below the TPA limit, and the use of a silicon–organic hybrid approach[11]. Lastly, limitations due to the choice of resonant configurations with a ring filter, grating or photonic crystal might add up.

Applications

The following section reviews a number of techniques that illustrate the potential of nonlinear silicon photonics for practical applications.

Supercontinuum generation: SPM. The generation of ultrabroadband spectra using SPM in a nonlinear fibre has already found useful applications in a wide variety of fields, including for optical coherence tomography[64], frequency metrology at unprecedented accuracy[65], all-optical signal regeneration demonstrating 40 Gbit s^{-1} transmission over as much as one million kilometres[66], and spectral slicing of wavelength-division multiplexing single-laser sources (for example, a recent experiment involved encoding a 10 Tbit s^{-1} signal in a single laser[67]). These applications have so far used optical powers in the range of 1 W and fibres with typical lengths of around 100 m. However, recent progress in silicon has allowed generation of a spectral supercontinuum of 350 nm width and beyond[68–71] in a single silicon wire waveguide of only a few centimetres in length. A recent experiment demonstrated continuum generation, spectral slicing and the dropping of several wavelengths on a single chip[72], the scheme for which is shown in Fig. 3a. The figure shows how a short laser pulse is spectrally broadened in a silicon wire waveguide 2 cm in length, and how it is subsequently dropped onto three outputs at different wavelengths using ring filters.

Green light emission: THG. The generation of green light through THG in silicon has long been of interest[73], with recent studies demonstrating the generation of green light in a slow-light silicon photonic crystal waveguide (Fig. 3b)[47]. The challenge in THG — which involves converting three photons of energy $\hbar\omega$ into a single photon of energy $3\hbar\omega$ — is to achieve the necessary conversion efficiency while making sure that the green light generated by THG is not absorbed in silicon. The success of the structure shown in Fig. 3b is due to several factors. First, a large enhanced electric field is present, resulting from the strong confinement of the silicon waveguide structure in combination with the pulse compression provided by the photonic crystal. Such an enhancement is beneficial because the third-harmonic conversion efficiency scales as the square of the pump intensity. Second, the photonic crystal is designed to emit the green light perpendicularly to the slow-light propagation direction, because otherwise the newly generated green light would be absorbed in silicon. This scheme was recently found to be useful for all-optical monitoring applications. It has been shown that the conversion efficiency for a particular input power directly relates to the optical signal-to-noise ratio. Experiments have been performed for signals of up to 640 Gbit s^{-1} (ref. 25).

Light amplification and lasing: The Raman effect. Silicon has the potential to provide cheap integrated optical components that can overcome their own internal losses using built-in amplifiers, or generate light on-chip. Unfortunately, the indirect bandgap of silicon means that it is inefficient in spontaneously emitting photons. Although one solution towards the realization of a silicon amplifier or laser is the use of silicon engineered materials[74], another promising path is to exploit stimulated Raman scattering (SRS). Raman gain and amplification beyond 11 dB has been reported for both the telecommunications window[12,74–82] and the mid-infrared wavelength region[45]. An advantage of Raman amplification is that it works well over a large spectral range. However, the Raman gain spectrum is narrow (1.2 nm), so amplification works well only for a single channel at most.

SRS lasing has also been demonstrated[83,84]. Figure 3c shows an instructive example of a silicon Raman laser on a single chip with a ring laser[84]. The silicon Raman laser chip comprises a 3 cm ring resonator with waveguide widths of w = 1.5 μm, heights of h = 1.55 μm and etch depths of 0.76 μm. The Raman pump and Raman-generated lasing signal are coupled in and out through a directional coupler. One of the main issues in Raman-pumped silicon lasers are the free-carrier related losses resulting from TPA. In this case, a p-i-n structure was placed along the waveguide rib to 'sweep out' these free carriers and thus reduce losses. A reverse bias of up to 25 V was applied along the junction, which had a width of 6 μm. When a pump laser of wavelength 1,550 nm was launched into the device, laser emission at 1,686 nm was observed. The threshold was found to be at a pump power of 20 mW, and the slope efficiency was close to 28%. Up to 50 mW of output power was measured with a reverse bias of 25 V across the junction, whereas a maximum of only 10 mW was achieved without a reverse bias. SRS has also been useful for tuning the slowdown factor of light in silicon[85].

Light amplification: FWM. Amplification in silicon has also been demonstrated using FWM[15,46,86]. Unlike the Raman effect, the FWM effect may provide broadband parametric amplification if phase-matching is achieved. The FWM amplification scheme typically involves two pump photons at ω_p passing their energy to a weaker signal ω_s and an idler signal ω_i such that the relation $2\omega_p = \omega_s + \omega_i$ holds. Amplification by FWM in silicon is an ultrafast parametric gain process. FWM-based parametric gain has a large gain bandwidth over tens of nanometres, which is a significant improvement over SRS gain. The challenge with FWM-based processes is that phase-matching must be maintained over the gain spectrum of interest, and this typically requires careful dispersion engineering. Parametric gain will only be observed for strong pump signals, leading to both SPM-induced refractive index changes for the pump signal itself and XPM-based refractive index modulations of the signal and idler waves. These changes must also be included in the phase-matching condition[15]. Successful parametric gain has been demonstrated around the communications wavelength of 1.55 μm (ref. 15) and in the mid-infrared[46,86], thanks to the small TPA coefficient in this region. The TPA coefficient is low in the mid-infrared because photon energies are lower than half the bandgap energy of silicon, and therefore TPA-related FCA effects do not result. Figure 4a shows the set-up of an experiment in which parametric gain in a silicon wire waveguide measuring 4 mm × 700 nm × 425 nm was achieved[46]. An on-chip gain of up to 25.4 dB was demonstrated around a wavelength of 2,220 nm with a gain bandwidth exceeding 220 nm (ref. 86). The dimensions were chosen to provide zero-dispersion at 2,260 nm, thus producing anomalous dispersion of 1,000 ps nm^{-1} km^{-1} around the pump wavelength at 2,170 nm. Pump pulses with a peak power of 27.9 W and with a repetition rate of 76 MHz were launched into the device, along with a continuous-wave (CW) signal of less than 0.45 mW. The idler conversion gain and the signal gain are plotted in Fig. 4b for various situations in which the signal was detuned from 2,060 nm to 2,280 nm.

Mid-infrared wavelength conversion based on FWM using compact fibre-based sources as the pump and probe has also been recently reported[87]. A maximum wavelength of 2,388 nm was obtained using a probe at 1,758 nm and a pump at 2,025 nm with a conversion efficiency of −36.8 dB.

It is worth mentioning here that recent work has demonstrated an optical parametric oscillator in a silicon nitride ring, and this

set-up has been used with optical pumping to reach more than 100 unprecedented wavelengths[88].

All-optical wavelength conversion: FWM/XPM. All-optical wavelength conversion based on FWM has been studied intensively in recent years, both in non-degenerate[1] and degenerate[2,89–92] schemes. Wavelength conversion is of interest in optical communications to overcome wavelength-blocking issues at network nodes. Conversion efficiencies of around −10 dB have been demonstrated for 10 Gbit s^{-1} wavelength conversion[90–92] and 10 Gbit s^{-1} signal regeneration[93]. By appropriate engineering of the waveguide dimensions, conversion over more than 150 nm has been achieved[92]. At higher data rates[2,94], TPA-generated free carriers accumulate, and the conversion efficiency suffers from free-carrier absorption. A reverse-biased p-i-n junction can be used to actively move free carriers out of the waveguide core, allowing for conversion efficiencies of around −8.6 dB at a data rate of 40 Gbit s^{-1} (ref. 2). However, two-photon-induced nonlinear loss still represents a problem in many all-optical signal processing applications. This problem can be avoided by using the SOH platform, in which the optical signal is guided by the silicon waveguides but the nonlinearity comes from an organic cladding material[41,49,3]. Pattern-free wavelength conversion has been demonstrated at 42.7 Gbit s^{-1} using a 4-mm-long SOH slot waveguide[95], and a more recent experiment demonstrated FWM-based wavelength conversion of a 56 Gbit s^{-1} DQPSK (differential quadrature phase shift keying) phase-encoded signal[96] — the first demonstration of phase-preserving wavelength conversion on a silicon chip. The experiment was performed with a SOH wire waveguide. The experimental set-up and eye diagram of the quadrature channel are shown in Fig. 4c. All-optical wavelength conversion can also be achieved by exploiting XPM. An advantage of XPM-based wavelength conversion over FWM-based all-optical wavelength conversion is its insensitivity to dispersion, which makes it easier to perform wavelength conversion over a large spectral range. In XPM schemes, a strong data signal leads to intensity-dependent refractive index changes in a co-propagating probe signal. Subsequent offset filtering is used to extract the converted signal. Format conversion of a 10 Gbit s^{-1} NRZ-OOK (non-return-to-zero on–off-keying) to RZ (return-to-zero) has been reported in conventional silicon nanowires[97], and a data rate of 42.7 Gbit s^{-1} has been reported for SOH slot waveguides[98]. Parametric wavelength conversion from 1,550 nm to 1,300 nm was also demonstrated for megabit-per-second optical signals using SRS[99]. The conversion efficiency was limited by imperfect phase-matching and the low-power CW pump, but could be increased to 58% by using pulsed pump light[100]. As a non-parametric effect, cross-TPA was investigated to achieve all-optical wavelength conversion[101]. In this approach, a strong data signal and a weak CW probe signal are launched into a silicon nanowire waveguide. The instantaneous photon density of the data signal induces TPA by pairs of data and probe photons, hence modulating the probe light. Cross-TPA itself is ultrafast, but the generated free carriers tend to accumulate, hence limiting the dynamic performance of the device.

All-optical demultiplexing: FWM. All-optical demultiplexing is frequently used to convert high-speed signals to lower bit-rates that can then be electronically processed. Experiments demonstrating the demultiplexing of 1.28 Tbit s^{-1} signals to 10 Gbit s^{-1} (ref. 4) and 160 Gbit s^{-1} to 10 Gbit s^{-1} (ref. 102) have been reported for silicon nananowires. Using the SOH approach, demultiplexing of 170.8 Gbit s^{-1} to 42.7 Gbit s^{-1} (ref. 3) and 120 Gbit s^{-1} to 10 Gbit s^{-1} (ref. 60) has been achieved.

Ultrafast oscilloscopes and waveform compression by means of FWM-assisted time-to-frequency conversion. By exploiting FWM in silicon waveguides and taking advantage of second-order dispersive fibres, optical time-to-frequency conversion and time-lenses have been demonstrated. A potential application is the realization of oscilloscopes that can magnify an ultrafast pulse sequence into a lower speed signal or that can demagnify a lower bit-rate signal into an ultrafast code.

The operating principle of time-to-frequency conversion and time lenses is traditionally explained using spacetime duality[5,103,104].

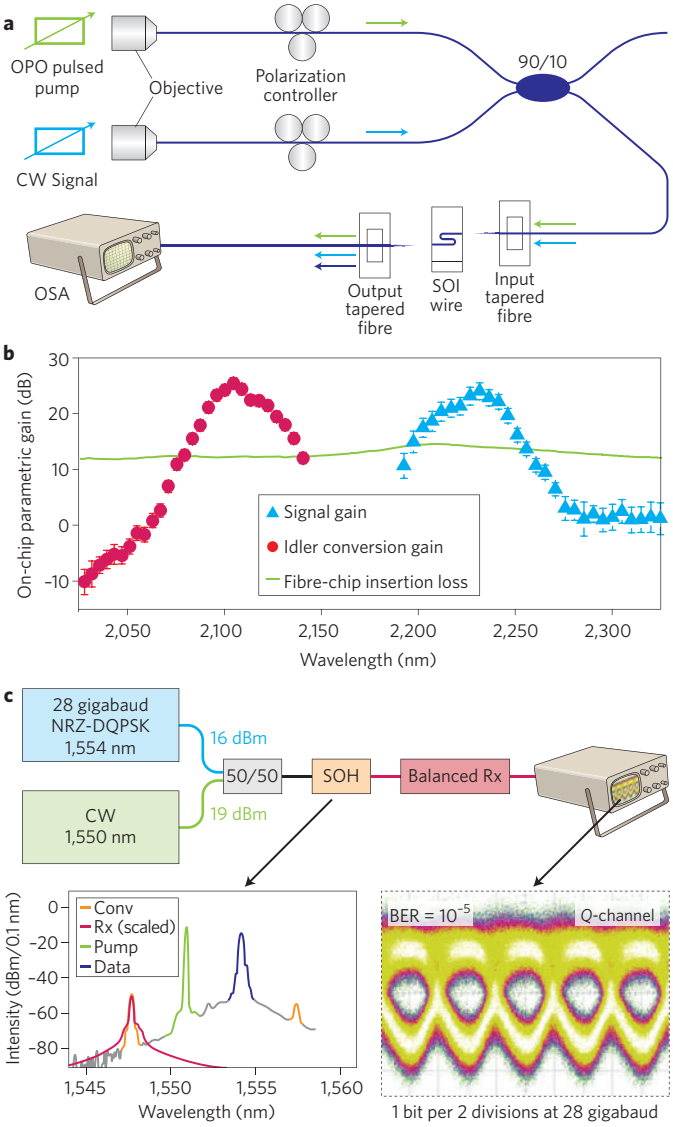

Figure 4 | Applications exploiting the FWM effect. a, Set-up exhibiting FWM-based parametric gain. A strong pulsed signal is launched into the silicon wire together with a continuous-wave signal. Energy is then transferred from the strong pump signal to the signal and idler signal, thereby providing amplification. **b**, Parametric gain coefficients of the signal and the conversion efficiency for the idler. OPO, optical parametric oscillator; OSA, optical spectrum analyser. **c**, All-optical wavelength conversion of a 56 Gbit s^{-1} DQPSK signal from 1,554 nm to 1,550 nm using FWM in a 4-mm-long silicon–organic hybrid (SOH) waveguide[96]. The spectra shows the NRZ DQPSK signal (blue), the continuous-wave signal (green) and the new wavelength converted signal (red), which was detected in a balanced received (Rx). The eye diagram shows open eyes for both the in- and quadrature-phase components. BER, bit-error rate. Figure reproduced with permission from: **a**, ref. 46, © IEEE 2009; **b**, ref. 86, © 2010 NPG.

NATURE PHOTONICS DOI: 10.1038/NPHOTON.2010.185

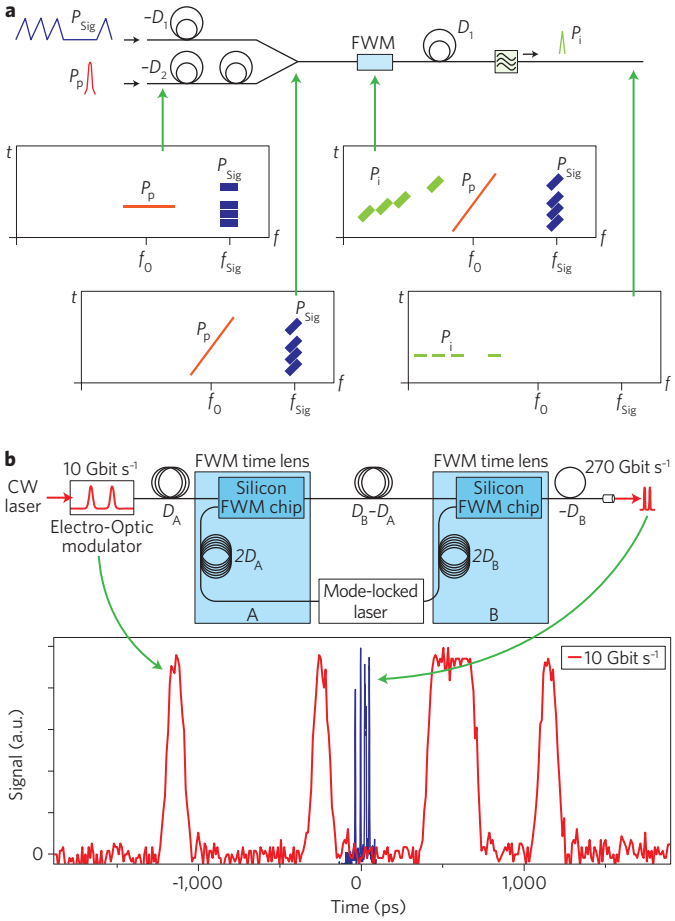

Figure 5 | Time-to-frequency conversion scheme and demonstration of a time lens. a, Operating principle of time-to-frequency conversion. The spectrograms show an ultrashort pulse P_p and the 10111 sequence P_{sig}. **b**, Set-up of a time lens comprising time-to-frequency (A) and frequency-to-time (B) schemes, each with different scaling factors, thus allowing both magnification and demagnification. The red pattern at the bottom was demagnified by a factor of 27 into the blue pattern. Figure **b** reproduced with permission from ref. 104, © 2009 NPG.

Here we attempt to give an alternative explanation of the time-to-frequency conversion concept. The conceptual experiment discussed here gives the conceptual framework, but not necessarily the subtleties. The time-to-frequency set-up comprises dispersive fibres with lengths larger than the respective dispersion lengths, so that the chirp (the dispersion-induced change of frequency with time) decreases with fibre length and dispersion D. A coupler and a nonlinear FWM element complete the set-up (Fig. 5a). Initially, a pulse sequence P_{in} and a single short pulse P_p are launched into dispersive fibres with negative accumulated total dispersion $-D_1$ and $-D_2$, respectively. The frequency–time spectrograms at the various positions within the set-up are plotted beneath the scheme. It can be seen from the first spectrogram that P_{in} and P_p are initially unchirped. After passing through the fibres, they both become chirped to different degrees. On performing FWM in the nonlinear element, an idler field $E_i = E_p^2 E_{sig}^*$ is generated from the pump and the signal fields E_p and E_{sig}, respectively. Because the amplitude of the pump field is squared, the pump chirp increases to the same amount as the signal chirp. As a result of FWM, at any point in time the spectral components of the idler all keep the same distance from the pump spectrum, making the idler spectrally spread as per the chirp of the involved pulses P_{sig} and P_p.

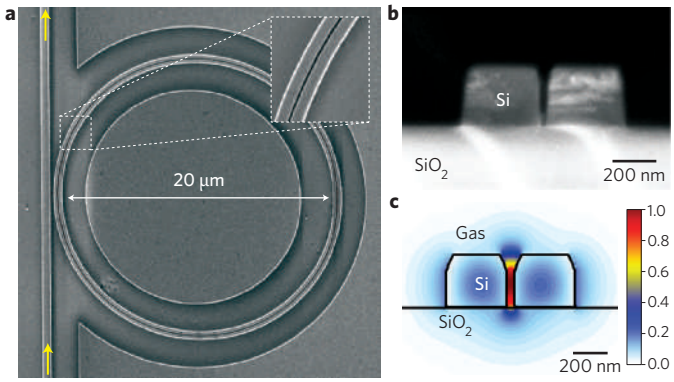

Figure 6 | Gas sensor. a, Scheme of a gas sensor comprising a slot microring resonator. **b**,**c**, Scanning electron microscope image (**b**) and optical transverse electric field distribution (**c**) in a slot waveguide. Scale shows the electric field intensity in arbitrary units. Figure reproduced with permission from ref. 7, © 2008 OSA.

Upon transmitting the idler through a fibre with a totally accumulated positive dispersion D_1, the dispersion is undone, and the pulses arrive all at the same time. Consequently, perfect time-to-frequency conversion is achieved.

Cascading time-to-frequency and frequency-to-time conversion schemes allows the generation of a temporal image of a pulse sequence that is either stretched or compressed in time[104]. This is a useful feature that allows an optical signal either to be sampled with limited-speed electronics or its bit-rate to be increased within a certain time window[5]. Figure 5b shows a temporal imaging system comprising a time-to-frequency conversion scheme with accumulated dispersion D_A and a frequency-to-time converter with accumulated dispersion $-D_B$. Cascading the two schemes results in a temporal image that is demagnified by a factor D_B/D_A. Figure 5b shows an initial 10 Gbit s^{-1} sequence being demagnified by a factor of 27 onto a 270 Gbit s^{-1} sequence.

Photonic sensors. These are likely to play an important role in all future silicon photonics devices[105]. Cheap and sensitive sensors are needed for industrial and public safety applications, as well as for personal use. In many cases optical sensors will be based on evanescent wave detection, in which a receptor layer on top of a core surface of a waveguide changes its optical properties upon reaction with a specific substance. This change is then detected through the evanescent field of the guided light, and its amplitude can be correlated to the concentration of the substance[106]. In the context of this Review, current research attention is on highly sensitive detectors that can detect the slightest changes in refractive index. An interesting approach is to combine high-Q ring resonators with the slotted waveguide approach[6,9,107]. Resonant ring filters have shown to be highly sensitive to small changes in refractive index, and the slot provides a good overlap of light with the substance to be probed. Such a scheme has recently been used to demonstrate a sensitive gas or pressure sensor[7] (Fig. 6). The sensor consisted of a 20 μm microring resonator with a Q-factor of ~5,000. The slotted waveguides were 600 nm wide and 250 nm tall, with a 40 nm slot. The authors were able to detect refractive index changes due to pressure of the order of 10^{-4} in the near-infrared.

Conclusions

This Review has given a summary of the nonlinearities of silicon and their respective applications. Silicon has convincingly demonstrated its ability to amplify, generate, process and sense signals. Although its low cost, compactness, mass-manufacturability and

compatibility with CMOS architecture are all key to bringing this technology to market, waveguide losses in some applications will need to be further reduced, and the development of CMOS integration processes will require further work. However, one can already envisage the introduction of all new ultracompact transceivers offering gigabit-per-second capacities on a device the size of a fingernail. It is foreseeable that optical interconnects, data communication and telecommunications will all take advantage of the new optical silicon chips. Ultimately, the realization of 'terabit-per-second on-chip' silicon processors seems to be possible. If successful, such devices will offer smaller footprint, lower energy consumption and lower cost than present non-silicon transceiver and only-electronic solutions. Furthermore, it is likely that new silicon laser sources and amplifiers that cover new spectral ranges will be added. In the near future, nonlinear silicon photonics could challenge state-of-the-art green lasers such as those used in laser pointers, and may eventually become competitors to quantum cascade lasers. As the field matures and prices come down, silicon optical sensors and silicon all-optical monitoring devices may become ubiquitous and affordable for mass-production.

References

1. Espinola, R. L., Dadap, J. I., Osgood, R. M., McNab, S. J. & Vlasov, Y. A. C-band wavelength conversion in silicon photonic wire waveguides. *Opt. Express* **13,** 4341–4349 (2005).
2. Kuo, Y., Rong, H., Sih, V., Xu, S. & Paniccia, M. Demonstration of wavelength conversion at 40 Gb/s data rate in silicon waveguides. *Opt. Express* **14,** 11721–11726 (2006).
3. Koos, C. *et al.* All-optical high-speed signal processing with silicon–organic hybrid slot waveguides. *Nature Photon.* **3,** 216–219 (2009).
4. Ji, H. *et al.* Optical waveform sampling and error-free demultiplexing of 1.28 Tbit/s serial data in a silicon nanowire. *Optical Fiber Communication Conf.* paper PDPC7 (2010).
5. Foster, M. A. *et al.* Silicon-chip-based ultrafast optical oscilloscope. *Nature* **456,** 81–85 (2008).
6. Dell'Olio, F. & Passaro, V. M. Optical sensing by optimized silicon slot waveguides. *Opt. Express* **15,** 4977–4993 (2007).
7. Robinson, J. T., Chen, L. & Lipson, M. On-chip gas detection in silicon optical microcavities. *Opt. Express* **16,** 4296–4301 (2008).
8. Tang, C. K. & Reed, G. T. Highly efficient optical phase modulator in SOI waveguides. *Electron. Lett.* **31,** 451–452 (1995).
9. Baehr-Jones, T. & Hochberg, M. Optical modulation and detection in slotted silicon waveguides. *Opt. Express* **13,** 5216–5226 (2005).
10. Brosi, J.-M. *et al.* High-speed low-voltage electro-optic modulator with a polymer-infiltrated silicon photonic crystal waveguide. *Opt. Express* **16,** 4177–4191 (2008).
11. Leuthold, J. *et al.* Silicon organic hybrid technology — a platform for practical nonlinear optics. *Proc. IEEE* **97,** 1304–1316 (2009).
12. Claps, R., Dimitropoulos, D., Raghunathan, V., Han, Y. & Jalali, B. Observation of stimulated Raman amplification in silicon waveguides. *Opt. Express* **11,** 1731–1739 (2003).
13. Liang, T. K. & Tsang, H. K. Efficient Raman amplification in silicon-on-insulator waveguides. *Appl. Phys. Lett.* **85,** 3343–3345 (2004).
14. Rong, H. *et al.* An all-silicon Raman laser. *Nature* **433,** 292–294 (2005).
15. Foster, M. A. *et al.* Broad-band optical parametric gain on a silicon photonic chip. *Nature* **441,** 960–963 (2006).
16. Tsuchizawa, T. *et al.* Microphotonics devices based on silicon microfabrication technology. *IEEE J. Sel. Top. Quant. Electron.* **11,** 232–240 (2005).
17. Bogaerts, W. *et al.* Compact wavelength-selective functions in silicon-on-insulator photonic wires. *IEEE J. Sel. Top. Quant. Electron.* **12,** 1394–1401 (2006).
18. Lipson, M. Guiding, modulating, and emitting light on silicon — challenges and opportunities. *J. Lightwave Technol.* **23,** 4222–4238 (2005).
19. Vlasov, Y. A. Silicon photonics for next generation computing systems. *Proc. 34th European Conf. Optical Communications* paper Tu.1.A.1 (2008).
20. Lee, B. G. & Bergmann, K. Silicon nano-photonic interconnection networks in multicore processor systems. *Proc. OSA Annual Meeting* paper FThS1 (2008).
21. Van Thourhout, D. *et al.* Photonic interconnect layer on CMOS. *Proc. 33rd European Conf. Optical Communications* paper 6.3.1 (2007).
22. Tsybeskov, L., Lockwood, D. J. & Ichikawa, M. Silicon photonics: CMOS going optical. *Proc. IEEE* **97,** 1161–1165 (2009).
23. Miller, D. Device requirements for optical interconnects to silicon chips. *Proc. IEEE* **97,** 1166–1185 (2009).
24. Krishnamoorthy, A. V. *et al.* Computer systems based on silicon photonic interconnects. *Proc. IEEE* **97,** 1337–1361 (2009).
25. Corcoran, B. *et al.* Optical signal processing on a silicon chip at 640 Gb/s using slow-light. *Opt. Express* **18,** 7770–7781 (2010).
26. Boyd, R. W. *Nonlinear Optics* 3rd edn (Academic Press, 2008).
27. Lin, Q., Painter, O. J. & Agrawal, G. P. Nonlinear optical phenomena in silicon waveguides: Modeling and applications. *Opt. Express* **15,** 16604–16644 (2007).
28. Osgood, R. M. Jr *et al.* Engineering nonlinearities in nanoscalse optical systems: Physics and applications in dispersion-engineered silicon nonaphotonics wires. *Adv. Opt. Photon.* **1,** 162–235 (2009).
29. Palik, E. D. *Handbook of Optical Constants of Solids* (Academic Press, 1998).
30. Foster, M. A., Turner, A. C., Lipson, M. & Gaeta, A. L. Nonlinear optics in photonic nanowires. *Opt. Express* **16,** 1300–1320 (2008).
31. Soref, R. A. & Bennett, B. R. Electrooptical effects in silicon. *IEEE J. Quant. Electron.* **QE-23,** 123–129 (1987).
32. Jacobsen, R. S. *et al.* Strained silicon as a new electro-optic material. *Nature* **441,** 199–202 (2006).
33. Hochberg, M. *et al.* Towards a millivolt optical modulator with nano-slot waveguides. *Opt. Express* **15,** 8401–8410 (2007).
34. Koos, C., Brosi, J.-M., Waldow, M., Freude, W. & Leuthold, J. Silicon-on-insulator modulators for next-generation 100 Gbit/s-Ethernet. *Proc. 33th European Conf. Optical Communications* paper P056 (2007).
35. Baehr-Jones, T. *et al.* Nonlinear polymer-clad silicon slot waveguide modulator with a half wave voltage of 0.25 V. *Appl. Phys. Lett.* **92,** 163303 (2008).
36. Liu, A. *et al.* A high-speed silicon optical modulator based on a metal-oxide-semiconductor capacitor. *Nature* **427,** 615–618 (2004).
37. Liao, L. *et al.* 40 Gbit/s silicon optical modulator for high-speed applications. *Electron. Lett.* **43,** 1196–1197 (2007).
38. Green, W. M., Rooks, M. J., Sekaric, L. & Vlasov, Y. A. Ultra-compact, low RF power, 10 Gb/s silicon Mach–Zehnder modulator. *Opt. Express* **15,** 17106–17113 (2007).
39. Xu, Q., Schmidt, B., Pradhan, S. & Lipson, M. Micrometre-scale silicon electro-optic modulator. *Nature* **435,** 325–327 (2005).
40. Liu, Y. & Tsang, H. K. Time dependent density of free carriers generated by two photon absorption in silicon waveguides. *Appl. Phys. Lett.* **90,** 211105 (2007).
41. Vallaitis, T. *et al.* Optical properties of highly nonlinear silicon-organic hybrid (SOH) waveguide geometries. *Opt. Express* **17,** 17357–17368 (2009).
42. Tsang, H. K. & Liu, Y. Nonlinear optical properties of silicon waveguides. *Semicond. Sci. Tech.* **23,** 064007 (2008).
43. Dinu, M. Dispersion of phonon-assisted nonresonant third-order nonlinearities. *IEEE J. Quant. Electron.* **39,** 1498–1503 (2003).
44. Sheik-Bahae, M. *et al.* Sensitive measurement of optical nonlinearities using a single beam. *IEEE J. Quant. Electron.* **26,** 760–769 (1990).
45. Raghunathan, V., Borlaug, D., Rice, R. R., Jalali, B. Demonstration of a mid-infrared silicon Raman amplifier. *Opt. Express* **15,** 14355–14362 (2007).
46. Liu, X., Osgood, R. M., Vlasov, Y. A. & Green, W. M. J. Broadband mid-infrared parametric amplification, net off-chip gain, and cascaded four-wave mixing in silicon photonic wires. *Proc. 6th IEEE Int. Conf. Group IV Photonics* pdp 1.3 (2009).
47. Corcoran, B. *et al.* Green light emission in silicon through slow-light enhanced third-harmonic generation in photonic crystal waveguides. *Nature Photon.* **3,** 206–210 (2009).
48. Foster, M. A., Moll, K. D. & Gaeta, A. L. Optimal waveguide dimensions for nonlinear interactions. *Opt. Express* **12,** 2880–2887 (2004).
49. Koos, C., Jacome, L., Poulton, C., Leuthold, J. & Freude, W. Nonlinear silicon-on-insulator waveguides for all-optical signal processing. *Opt. Express* **15,** 5976–5990 (2007).
50. Salem, R. *et al.* Signal regeneration using low-power four-wave mixing on silicon chip. *Nature Photon.* **2,** 35–38 (2008).
51. Michinobu, T. *et al.* A new class of organic donor–acceptor molecules with large third-order optical nonlinearities. *Chem. Commun.* 737–739 (2005).
52. Esembeson, B. *et al.* A high optical quality supramolecular assembly for third-order integrated nonlinear optics. *Adv. Mater.* **20,** 4584–4587 (2008).
53. May, J. C., Biaggio, I., Bures, F. & Diederich, F. Extended conjugation and donor–acceptor substitution to improve the third-order optical nonlinearity of small molecules. *Appl. Phys. Lett.* **90,** 251106 (2007).
54. Hales, J. M. & Perry, J. W. *Introduction to Organic Electronic and Optoelectronic Materials and Devices* (eds Sun, S.-S. & Dalton, L.) 521–579 (CRC, 2008).
55. Leong, J. Y. Y. *et al.* A lead silicate holey fiber with $\gamma = 1860$ W^{-1} km^{-1} at 1550 nm. *Optical Fiber Communication Conf.* paper PDP22 (2005).
56. Mägi, E. C. *et al.* Enhanced Kerr nonlinearity in sub-wavelength diameter As_2Se_3 chalcogenide fiber tapers. *Opt. Express* **15,** 10324–10329 (2007).

57. Hochberg, M. *et al.* Terahertz all-optical modulation in a silicon–polymer hybrid system. *Nature Mater.* **5,** 703–709 (2006).
58. Baehr-Jones, T. W. & Hochberg, M. J. Polymer silicon hybrid systems: A platform for practical nonlinear optics. *J. Phys. Chem. C* **112,** 8085–8090 (2008).
59. Almeida, V. R., Xu, Q., Barrios, C. A. & Lipson, M. Guiding and confining light in void nanostructure. *Opt. Lett.* **29,** 1209–1211 (2004).
60. Koos, C. *et al.* Highly-nonlinear silicon photonics slot waveguide. *Optical Fiber Communication Conf.* paper PDP25 (2008).
61. Soljacic, M. *et al.* Photonic-crystal slow-light enhancement of nonlinear phase sensitivity *J. Opt. Soc. Am. B* **19,** 2052–2059 (2002).
62. Gu, L., Jiang, W., Chen, X., Wang, L. & Chen, R. T. High speed silicon photonic crystal waveguide modulator for low voltage operation. *Appl. Phys. Lett.* **90,** 071105 (2007).
63. Turner, A. C. *et al.* Tailored anomalous group-velocity dispersion in silicon channel waveguides. *Opt. Express* **14,** 4357–4362 (2006).
64. Hartl, I. *et al.* Ultrahigh-resolution optical coherence tomography using continuum generation in an air silica microstructure optical fiber. *Opt. Lett.* **26,** 608–610 (2001).
65. Diddams, S. A. *et al.* Direct link between microwave and optical frequencies with a 300 THz femtosecond laser comb. *Phys. Rev. Lett.* **84,** 5102–5105 (2000).
66. Raybon, G. *et al.* 40 Gbit/s pseudo-linear transmission over one million kilometres. *Optical Fiber Communication Conf.* paper FD10 (2002).
67. Hillerkuss, D. *et al.* Single source optical OFDM transmitter and optical FFT receiver demonstrated at line rates of 5.4 and 10.8 Tbit/s. *Optical Fiber Communication Conf.* paper PDPC1 (2010).
68. Tsang, H. K. *et al.* Optical dispersion, two-photon absorption and self-phase modulation in silicon waveguides at 1.5μm wavelength. *Appl. Phys. Lett.* **80,** 416–418 (2002).
69. Rieger, G. W., Virk, K. S. & Young, J. F. Nonlinear propagation of ultrafast 1.5 μm pulses in high-index-contrast silicon-on-insulator waveguides. *Appl. Phys. Lett.* **84,** 900–902 (2004).
70. Yin, L., Lin, Q. & Agrawal, G. P. Soliton fission and supercontinuum generation in silicon waveguides. *Opt. Lett.* **32,** 391–393 (2007).
71. Hsieh, I. *et al.* Supercontinuum generation in silicon photonic wires. *Opt. Express* **15,** 15242–15249 (2007).
72. Koonath, P., Solli, D. R. & Jalali, B. Continuum generation and carving on a silicon chip. *Appl. Phys. Lett.* **91,** 061111 (2007).
73. Wang, C. C. *et al.* Optical third harmonic generation in reflection from crystalline and amorphous samples of silicon. *Phys. Rev. Lett.* **57,** 1647–1650 (1986).
74. Dal Negro, L. Light emission from silicon nanostructures: Past, present and future perspectives. *Proc. CLEO 2009* paper CTuN1 (2009).
75. Espinola, R., Dadap, J., Osgood, R. Jr, McNab, S. & Vlasov, Y. Raman amplification in ultrasmall silicon-on-insulator wire waveguides. *Opt. Express* **12,** 3713–3718 (2004).
76. Liu, A., Rong, H., Paniccia, M., Cohen, O. & Hak, D. Net optical gain in a low loss silicon-on insulator waveguide by stimulated Raman scattering. *Opt. Express* **12,** 4261–4267 (2004).
77. Xu, Q., Almeida, V. & Lipson, M. Time resolved study of Raman gain in highly confined silicon-on-insulator waveguides. *Opt. Express* **12,** 4437–4442 (2004).
78. Jalali, B., Raghunathan, V., Boyraz, O., Claps, R. & Dimitropoulos, D. Wavelength conversion and light amplification in silicon waveguides. *Proc. Int. Conf. Group IV Photonics* paper WA3 (2004).
79. Jones, R. *et al.* Net continuous wave optical gain in a low loss silicon-on-insulator waveguide by stimulated Raman scattering. *Opt. Express* **13,** 519–525 (2005).
80. Liu, Y. & Tsang, H. K. Nonlinear absorption and Raman gain in helium ion implanted silicon. *Opt. Lett.* **31,** 1714–1716 (2006).
81. Fathpour, S., Tsia, K. K. & Jalali, B. Energy harvesting in silicon Raman amplifiers. *Appl. Phys. Lett.* **89,** 061109 (2006).
82. Sih, V. *et al.* Raman amplification of 40Gb/s data in low-loss silicon waveguides. *Opt. Express* **15,** 357–362 (2007).
83. Boyraz, O. & Jalali, B. Demonstration of a silicon Raman laser. *Opt. Express* **12,** 5269–5273 (2004).
84. Rong, H. *et al.* Low-threshold continuous-wave Raman silicon laser. *Nature Photon.* **1,** 232–237 (2007).
85. Okawachi, Y. *et al.* All-optical slow-light on a photonic chip. *Opt. Express* **14,** 2317–2322 (2006).
86. Liu, X., Osgood, R. M., Vlasov, J. A. & Green, W. M. J. Mid-infrared optical parametric amplifier using silicon nanophotonic waveguides. *Nature Photon.* **4,** 557–560 (2010).
87. Zlatanovic, S. *et al.* Mid-infrared wavelength conversion in silicon waveguides using ultracompact telecom-band-derived pump source. *Nature Photon.* **4,** 561–564 (2010).
88. Levi, J. S. CMOS-compatible multiple-wavelength oscillator for on-chip optical interconnects. *Nature Photon.* **4,** 37–40 (2010).
89. Fukuda, H. *et al.* Four-wave mixing in silicon wire waveguides. *Opt. Express* **13,** 4629–4637 (2005).
90. Yamada, K. *et al.* All-optical efficient wavelength conversion using silicon photonic wire waveguide. *IEEE Photon. Tech. Lett.* **18,** 1046–1048 (2006).
91. Rong, H. S., Kuo, Y. H., Liu, A. S., Paniccia, M. & Cohen, O. High efficiency wavelength conversion of 10Gb/s data in silicon waveguides. *Opt. Express* **14,** 1182–1188 (2006).
92. Foster, M. A, Turner, A. C., Salem, R., Lipson, M. & Gaeta, A. L. Broad-band continuous-wave parametric wavelength conversion in silicon nanowaveguides. *Opt. Express* **15,** 12949–12958 (2007).
93. Salem, R. *et al.* Signal regeneration using low-power four-wave mixing on silicon chip. *Nature Photon.* **2,** 35–38 (2008).
94. Lee, B. G. *et al.* Demonstration of broadband wavelength conversion at 40 Gb/s in silicon waveguides. *IEEE Photon. Tech. Lett.* **21,** 182–184 (2009).
95. Vallaitis, T. *et al.* All-optical wavelength conversion at 42.7 Gbit/s in a 4 mm long silicon-organic hybrid waveguide. *Optical Fiber Communication Conf.* paper OWS3 (2009).
96. Vallaitis, T. *et al.* All-optical wavelength conversion of 56 Gbit/s NRZ-DQPSK signals in silicon–organic hybrid strip waveguides. *Optical Fiber Communication Conf.* paper OTuN1 (2010).
97. Astar, W. *et al.* Conversion of 10 Gb/s NRZ-OOK to RZ-OOK utilizing XPM in a Si nanowire. *Opt. Express* **17,** 12987–12999 (2009).
98. Vallaitis, T. *et al.* All-optical wavelength conversion using cross-phase modulation at 42.7 Gbit/s in silicon-organic hybrid (SOH) waveguides. *Proc. IEEE Int. Conf. Photonics in Switching 2009* 78–79 (2009).
99. Raghunathan, V., Claps, R., Dimitropoulos, D. & Jalali, B. Wavelength conversion in silicon using Raman induced four-wave mixing. *Appl. Phys. Lett.* **85,** 34–36 (2004).
100. Koonath, P., Solli, D. R. & Jalali, B. High efficiency CARS conversion in silicon. *Conf. Lasers and Electro-optics & Quantum Electronics and Laser Science* paper CThE3 (2008).
101. Moss, D. J., Fu, L., Littler, I. & Eggleton, B. J. Ultrafast all-optical modulation via two-photon absorption in silicon-insulator waveguides. *Electron. Lett.* **41,** 320–321 (2005).
102. Li, F. *et al.* Error-free all-optical demultiplexing at 160Gb/s via FWM in a silicon nanowire. *Opt. Express* **18,** 3905–3910 (2010).
103. Azna, J. Time-to-frequency conversion using a single time lens. *Opt. Commun.* **217,** 205–209 (2003).
104. Foster, M. A. *et al.* Ultrafast waveform compression using a time-domain telescope. *Nature Photon.* **3,** 581–585 (2009).
105. Pavesi, L. & Lockwood, D. J. *Silicon Photonics* (Springer, 2004).
106. Zinoviev, K. *et al.* Silicon photonic biosensors for lab-on-a-chip applications. *Adv. Opt. Technol.* 383927 (2008).
107. Baehr-Jones, T., Hochberg, M., Walker, C. & Scherer, A. High-Q optical resonators in silicon-on-insulator-based slot waveguides. *Appl. Phys. Lett.* **86,** 081101 (2005).

Acknowledgements

This work was in part supported by the Center for Functional Nanostructures (CFN) funded by the German science foundation (DFG), the European project SOFI and the European project EURO-FOS.

Additional information

The authors declare no competing financial interests.